

# Thin-film piezoelectric and high-aspect ratio polymer leg mechanisms for millimeter-scale robotics

Jongsoo Choi<sup>1</sup> · Minchul Shin<sup>2</sup> · Ryan Q. Rudy<sup>3</sup> · Christopher Kao<sup>1</sup> · Jeffrey S. Pulskamp<sup>3</sup> · Ronald G. Polcawich<sup>3</sup> · Kenn R. Oldham<sup>1</sup>

Received: 11 October 2016 / Accepted: 22 March 2017 / Published online: 24 April 2017  
© Springer Singapore 2017

**Abstract** Millimeter-scale micro-robotic leg actuators are described that integrate thin-film lead zirconate titanate (PZT) piezoelectric actuation with compliant structures formed from parylene-C polymer. Models for out-of-plane rotation using piezoelectric cantilevers and in-plane rotation using high-aspect ratio polymer beams are discussed. Opportunities are highlighted for thin polymer films to aid in load-bearing, flexibility, and resilience of piezoelectric micro-robot appendages. A simple 5 mm × 2.4 mm × 0.15 mm hexapod robot prototype incorporating multiple actuators in each leg assembly is fabricated and tested within the silicon wafer in which it was built. Completed robot leg performance shows close agreement between modeled and tested static and dynamic characteristics, with potential benefits for future walking micro-robots from low power requirements relative to payload capacity and large amplitude motion at resonance.

**Keywords** Micro-robotics · Piezoelectric actuation · Microfabrication · Compliant mechanisms

## 1 Introduction

The term “micro-robot” has been applied to a wide range of small robotic systems, from roughly hand-sized robots based on conventional actuators and manufacturing processes to entire robots just microns in size reliant primarily

on external stimuli to generate motion. Micro-robotic systems specifically originating in the field of micro-electromechanical systems, or MEMS, are typically characterized by their minimum feature sizes being at the micron-scale, and overall size on the order of a few millimeters to a centimeter. Conceptually, MEMS technology applied to robotic applications could provide means to closely integrate actuation, sensing, electronics and power systems for applications requiring sensing or manipulation in small spaces, such as searching disaster sites, monitoring infrastructure, or performing reconnaissance. In practice, functionality of millimeter-scale micro-robots remains limited, particularly with respect to autonomous locomotion given actuator, power, and integration challenges.

Legged robots at the millimeter-to-centimeter scale, the focus of this work, have been demonstrated based on a variety of transduction methods. These include electrothermal (Ebefors 1999; Erdem et al. 2010; Murthy et al. 2012), electrostatic (Hollar et al. 2005), shape-memory alloy (Sugita et al. 2016), electroactive polymer (Kim et al. 2003), and piezoelectric (Sanuy et al. 2008) actuation. Locomotion speeds remain low, however, and are typically limited to occur over very smooth or well-defined surfaces, mostly due to either power or actuation constraints. Electrothermal, SMA, and electroactive polymer actuators tend to have limited bandwidth and require either large voltages or currents. Electrostatic actuators typically provide limited force and bulk ceramic piezoelectric actuators have limited stroke lengths, both while requiring large voltages. Thin-film piezoelectric actuators, relative to other micro-scale actuators, have potential to generate large forces ( $10^{-1}$ – $10^{-3}$  N) at relatively high bandwidth ( $10^2$ – $10^3$  Hz), with modest voltage and power requirement. However, stroke lengths, especially in translation, tend to be small, making it challenging to integrate the thin film actuators with

✉ Kenn R. Oldham  
oldham@umich.edu

<sup>1</sup> University of Michigan, Ann Arbor, USA

<sup>2</sup> Georgia Southern University, Statesboro, GA, USA

<sup>3</sup> U.S. Army Research Laboratory, Adelphi, MD, USA

other structures, and the resulting structures are often quite fragile.

This paper focuses on potential benefits of thin-film piezoelectric microactuators with high-aspect polymers in micro-robotic leg joint mechanisms. An example of an early robot prototype with schematic views of in-plane and out-of-plane actuation mechanisms is shown in Fig. 1. Such mechanisms take advantage of both the high work density of piezoelectric actuation and the resilient, highly-compliant nature of polymers used in microfabrication, at least relative to metal and semiconductor materials common in MEMS.

Due to their very different processing requirements, integration of polymer structures with thin-film piezoelectric ceramics is rare, though examples of co-fabrication do exist. For example, polymer films have been tested as protective encapsulation of PZT (Guerre et al. 2010), as PZT micromolds (Navarre et al. 2007; Park et al. 2003), for improving properties of complementary layers in acoustic transducers (Dellmann et al. 1997), to carry large numbers of electrical interconnects across PZT beams (Aktakka et al. 2014) and to tailor damping properties of a piezoelectric accelerometer (Nemirovsky et al. 1996). However, in these applications polymer materials are not playing a key structural role in generating motion. Actuation devices based on polymer-PZT integration include a micro-pump (Luo et al. 2011) and mechanisms based on SU-8 photo-polymer for amplifying piezoelectric displacements (Conway et al. 2007), but in these cases the piezoelectric element was a manually-assembled, cut ceramic block. Much research has also been performed on piezoelectric polymers for micro-scale devices (Kim et al. 2003; Fu et al. 2005; Lam et al. 2005), but energy density of such materials is much smaller than that of PZT and related ceramics.

At larger scales, PZT or other piezoelectric ceramics have been used in a variety of polymer-based composites (Venkatragavaraj et al. 2000; Ritter et al. 2002), but with limited geometries available for micro-scale devices.

Piezoelectric and polymers materials have also seen significant use in prior micro-robots. At the millimeter scale, polymers have served as energy storage mechanisms for jumping (Bergbreiter and Pister 2007), to increase thermal actuator displacement (Ebefors et al. 1999). At slightly larger scales ( $\sim 2\text{--}10\text{ cm}$ ), polymer and piezoelectric laminates have found great success in flying robots (Ma et al. 2013). Also at that scale, elastomeric leg mechanisms have been used for high-speed walking locomotion (Vogtmann et al. 2011), and simple 3D-printed polymer robots with bulk ceramic PZT have been used to explore small-scale contact dynamics (Qu and Oldham 2016). Other centimeter-scale bulk ceramic piezoelectric legged robots have been fabricated by laser-cutting or conventional machining (Hariri et al. 2016; Rios et al. 2016).

A benefit of using thin-film, rather than bulk ceramic, piezoelectric actuation in micro-robots is that large electric fields can be generated at much lower voltages, but robot development has to date been done mostly at the appendage level. Thin-film PZT bending beam have been used entirely for compliant elements in multiple axis robotic leg joints, through stress engineering to orient actuators in varying planes, as well as to create millimeter-scale wing structures (Pulskamp 2012). The authors have previously examined individual (Edamana et al. 2011) and multiple-degree-of-freedom (Rhee et al. 2012) thin-film PZT actuation structures based on complex, compliant silicon mechanisms. However, weight-bearing capabilities of these designs remained low and yield of completed robot legs too low for eventual multi-legged robot completion.

**Fig. 1** **a** Example of a 30-legged “millipede” micro-robot fabricated from a silicon wafer with thin-film piezoelectric actuators integrated into each leg; **b** schematic top-view of a single robot leg showing locations of high-aspect ratio polymer flexures and tethers for generating in-plane rotation, as well as thin-film piezoelectric unimorphs for actuation of both in-plane and out-of-plane motion; **c** schematic oblique view of fabricated leg structure

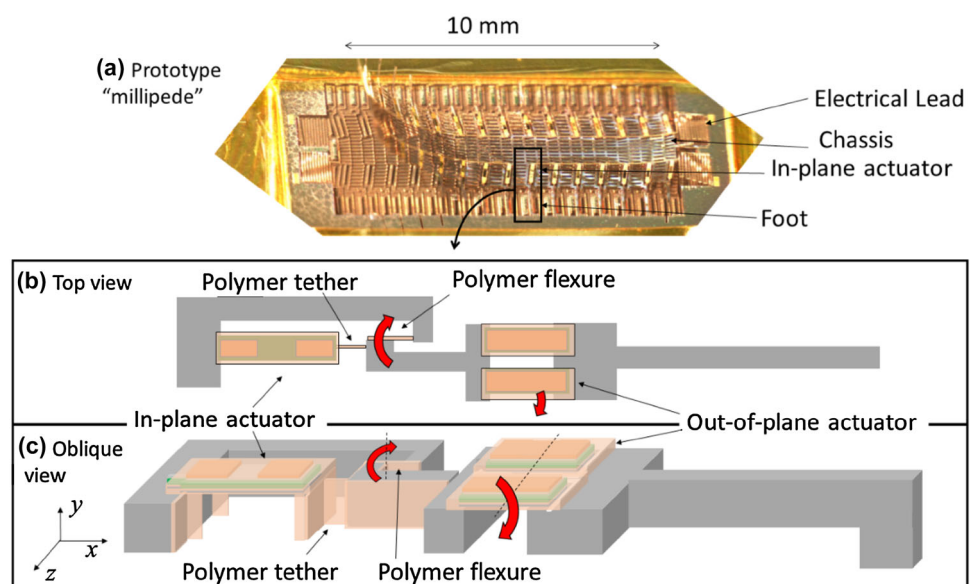
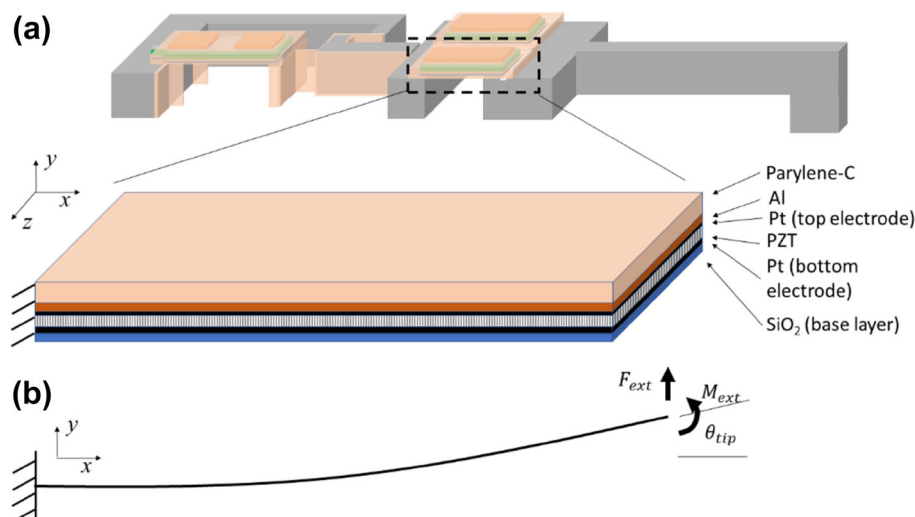


**Fig. 2** **a** Oblique view of generic thin-film piezoelectric leg architecture with expanded laminate out-of-plane bending structure (not to scale); **b** schematic beam bending geometry and load definitions



In this work, models for actuation assemblies generating both out-of-plane and in-plane motion are discussed when thin-film PZT is complemented with parylene-C films. High-aspect ratio parylene-C structures are fabricated by methods similar to that of Suzuki and Tai for non-piezoelectric accelerometer manufacturing (Suzuki and Tai 2006), and anisotropic parylene etching has been previously reported by Selvaraseh (Selvarasah et al. 2007). High-aspect ratio parylene-C processing in this work supports piezoelectric film integration, with preliminary mechanical property testing and actuator designs first reported by Shin et al. (2014). Mechanism performance in this paper is evaluated for multi-actuator legs that are integrated into simple robot prototypes, primarily a 5 mm × 2.4 mm × 0.15 mm hexapod design tested within a silicon chip.

## 2 Actuator and leg design

Elastic leg joints based on thin-film piezoelectric actuation for both out-of-plane and in-plane rotation are discussed in this section, introducing basic mechanism design then examining potential advantages of incorporating a polymer thin-film, in this case parylene-C, into such actuators.

### 2.1 Out-of-plane rotation: piezoelectric cantilevers

The basic actuation unit of a thin-film piezoelectric device is typically a multi-layer, unimorph beam or membrane containing the piezoelectric layer between two metal electrodes. High-quality piezoelectric thin-films generally require careful surface treatment before deposition, so a common laminate might consist of an elastic layer, bottom electrode, piezoelectric film, and top electrode, often with

additional seed and/or adhesion layers. This work uses an elastic or base layer of silicon dioxide followed by a titanium/platinum bottom electrode, PZT (52/48) layer, and platinum top electrode, shown schematically in Fig. 2a. An additional metal layer, such as gold or aluminum, may be selectively added to further strengthen the laminate, for reasons such as manipulating the neutral axis of the beam, improving beam stiffness, or incorporating bond pads. The entire cantilever may also be coated with parylene-C polymer, used to produce high-aspect ratio compliant links elsewhere in the MEMS devices.

Simple piezoelectric cantilevers can directly generate out-of-plane bending motion when an electric field is applied across the piezoelectric layer. This cantilever bending is also the primary mechanism for producing out-of-plane rotation for proposed micro-robotic leg designs discussed in this paper.

For beams that are thin relative to beam length and operate over small deflections, static piezoelectric cantilever deflection is well described by Bernoulli beam theory, which predicts out of plane tip rotation,  $\theta_{tip}$ , as.

$$\theta_{tip} = \frac{L}{(EI)_{comp}} (M_{act} + M_{ext}) + \frac{L^2}{2(EI)_{comp}} F_{ext} \quad (1)$$

where  $L$  is the length of the beam,  $(EI)_{comp}$  is the composite modulus of the laminate stack [see for example (Wang and Cross 1999)],  $M_{act}$  is the internal moment generated by the piezoelectric film, and  $M_{ext}$  and  $F_{ext}$  are external moment and vertical force on the beam, respectively, as shown in Fig. 2b. The internal bending moment generated by the film is determined by the applied voltage,  $V$ , effective electroactive piezoelectric strain coefficient at that voltage,  $d_{31,eff}$ , and offset between the height of the PZT film in the beam,  $y_{PZT}$ , and the beams neutral axis,  $\bar{y}$ , according to.

$$M_{act} = d_{31,eff}(V) \frac{V}{t_{PZT}} E_{PZT}(wt_{PZT})(y_{PZT} - \bar{y}) \quad (2)$$

where thickness of the PZT,  $t_{PZT}$ , beam width,  $w$ , and PZT elastic modulus,  $E_{PZT}$ , determine how free-strain of the PZT layer is related to equivalent internal axial force within the beam.

Several phenomena related to use of a piezoelectric thin-film, as opposed to bulk ceramic piezoelectric materials common at larger scales, are worth noting. First, due to the very small film thickness (on the order of 1  $\mu\text{m}$  or less), electric fields across the PZT exceed the coercive field for the material at just a few volts. Thus, unidirectional voltages are usually applied, as significant negative voltages (treating the initial poling voltage as positive) will re-orient the piezoelectric film. Second, the large electric fields result in substantial nonlinearity in strain vs. field, so an empirically-measured, voltage-dependent, effective piezoelectric coefficient,  $d_{31,eff}$ , is used in place of a constant linear piezoelectric coefficient. Hysteresis in the thin-film is modest, on the order of 10% of actuator amplitude or less.

Figure 3 displays trends in blocking force ( $\theta_{rip} = 0$ ,  $M_{ext} = 0$ ) and absolute tip rotation ( $F_{ext} = 0$ ,  $M_{ext} = 0$ ) for

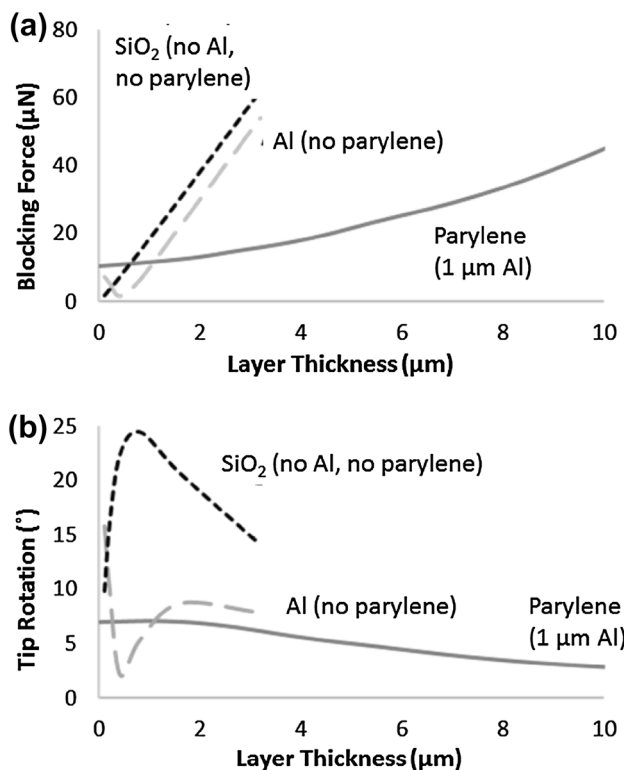


**Fig. 3** Analytical results for **a** blocking force and **b** tip angle for a 300  $\mu\text{m}$  long, 100  $\mu\text{m}$  wide PZT beam with layers shown in Fig. 2, as a function of layer thickness for either: SiO<sub>2</sub> (no metal or polymer reinforcement), Al (0.5  $\mu\text{m}$  SiO<sub>2</sub>, no polymer), or parylene-C (0.5  $\mu\text{m}$  SiO<sub>2</sub>, 1.0  $\mu\text{m}$  Al)

a 300  $\mu\text{m}$  long, 100  $\mu\text{m}$  wide beam at 20 V as a function of select layer thicknesses under three scenarios: using the initial piezoelectric stack layers alone (SiO<sub>2</sub> through top Pt electrode), adding a metal reinforcement layer of aluminum, and further increasing beam thickness with a parylene-C coating over 1  $\mu\text{m}$  of aluminum. Nominal layer thicknesses and other properties are listed in Table 1; effective piezoelectric coefficient at 20 V is taken to be approximately  $-120$  pC/N.

Generally speaking, as passive layers in the beam are made thicker, blocking force increases while bending angle decreases. However, because the height of the neutral axis of the beam and its composite modulus are not directly proportional, these trends are not necessarily monotonic. Relatively thick, low-modulus layers such as parylene-C, for example, affect composite modulus more significantly than neutral axis position. For the sample configurations in Fig. 3, a beam coated with a 5–10  $\mu\text{m}$  parylene layer can maintain blocking forces comparable to beams that would require 2–3  $\mu\text{m}$  of SiO<sub>2</sub> or Au. While the associated range of motion is reduced by 20–60%, large load-bearing is critical for walking micro-robots, and parylene films can be deposited to the thicknesses in question with lower residual stresses and lower probability of fracture failure. These benefits are not unique to parylene; several other polymers used in MEMS devices could provide similar advantages, but nevertheless complement the use of parylene-C for in-plane elastic bending elements, described in the following sections.

## 2.2 In-plane rotation: high-aspect ratio beam properties

The main benefit of using high-aspect ratio polymer materials in micro-robot leg joints is to enhance load-bearing of in-plane bending beams under actuation constraints. As a simple illustration, consider the length,  $L_{req}$ , of a uniform rectangular beam required to achieve a specified bending angle,  $\theta_d$ , with a given actuation moment,  $M_d$ , under Bernoulli beam bending assumptions,

**Table 1** Nominal PZT stack materials and moduli used in actuator modeling

Material	Thickness ( $\mu\text{m}$ )	Elastic modulus used in model (GPa)
Silicon dioxide	0.5	65
Platinum (bottom)	0.2	170
PZT (52/48)	1.0	70
Platinum (top)	0.1	170
Aluminum	1.0	69
Parylene-C	5.3	3

$$L_{req} = E_b \left( \frac{1}{12} w_b^3 t_b \right) \frac{\theta_d}{M_d} \tag{3}$$

where  $E_b$  is the elastic modulus of the beam, and  $w_b$  and  $t_b$  are its length and thickness, respectively. The maximum load force,  $F_y$ , that can be supported in the transverse direction while ensuring out-of-plane rotation below a maximum permissible transverse deflection angle,  $\phi_d$ , is given by.

$$F_y = \frac{2E_b \left( \frac{1}{12} w_b t_b^3 \right)}{L_{req}^2} \phi_d = \left( \frac{M_d}{\theta_d} \right)^2 \frac{24r}{E_b w_b^4} \phi_d \tag{4}$$

where the right hand term is obtained by applying (3) to compute  $L_{req}$ , and  $r$  is the aspect ratio of the beam,  $r = t_b/w_b$ . Equation (4) and the assumptions made above can be read as indicating that when:

- finite actuation moments are available, and,
- out-of-plane vs. in-plane deflection must be constrained,

then, transverse load bearing, i.e. robot payload capacity, is increased by using:

- materials with a low elastic modulus, and/or,
- materials with high aspect ratio and small minimum beam width (which are typically associated with one another in micro-machining processes).

The above analysis is, of course, simplistic. For one, Bernoulli bending models lose accuracy when beams can be made very thick relative to their length, either through high aspect ratios or short beam lengths. In addition, loading conditions for real robots are more complex than just a force at the end of a beam. For example, if out-of-plane translation is a stricter constraint than rotation, keeping elastic modulus low to allow small beam lengths becomes more important, while if body weight acts more as moment arm from the end of a long leg, aspect ratio becomes more important. Nonetheless, in general a robot relying on elastic beam deflection to generate motion is likely to accommodate smaller joints and actuators if constructed from low modulus materials, and support greater weights when those materials can be fabricated with high aspect ratios.

With those traits in mind, a variety of materials compatible with high-aspect ratio micro-fabrication are compared in Table 2. Out-of-plane stiffness (°/N) is calculated for a 5 μm beam long enough to produce 5° of bending with a 10 nN-m torque (approximately the conditions for in-plane actuators described later in this paper). Also shown are the minimum curvature achievable from a 5 μm wide beam, based on yield stress and elastic moduli of the materials, and the bending moment required to achieve that

**Table 2** Comparison of selected materials having available high-aspect ratio micro-fabrication processes

Material	Elastic modulus	Strain at failure	Representative yield stress	Max. aspect ratio	Transverse stiffness (mN/°) for beam 5° rotation with 10 nN-m actuation moment.	Minimum radius of curvature, 5 μm wide beam.	Moment required to achieve minimum radius of curvature
Si	165	0.1–2	300 (Wilson et al. 1996)	97:1 (DRIE) (Owen et al. 2012)	5	1375	4170
SiO <sub>2</sub>	65	0.6 (Sharpe et al. 2006)	365 (Sharpe et al. 2006)	20:1 (RIE) (Shareef et al. 1995)	2.7	445	1050
Au	55	10–20 (Timpiano 2005)	240 (Espinosa and Prorok 2003)	10:1 (TEOS refill) 90:1 (microcasting) (Baumeister et al. 2002) >50:1 (LIGA) (Rasmussen et al. 2003)	8	573	2406
SU-8	4.95	1–3 (Robin and Vishnoi 2013)	34 (Dellmann et al. 1997)	50:1 (lithography) (Liu et al. 2005)	89	364	244
PMMA	3.8 (Ash et al. 2001)	30–50 (Ash et al. 2001)	75 (Ash et al. 2001)	>50:1 (X-ray lithography) 20:1 (UV lithography)	115	127	752
Parylene-C	3	50–200 (Lu 2012)	60 (Lu 2012)	19:1 (embossing) (Becker and Heim 2000) <b>23:1 (this work)</b> <b>10:1 (hard mask RIE)</b>	67	127	216
						<b>125</b>	<b>198</b>

RIE, reactive-ion etching; TEOS, tetraethyl orthosilicate; LIGA, lithographic, galvanofarming, abforming; UV, ultraviolet light

curvature. Silicon, for example, is commonly machined to very high aspect ratios by deep-reactive-ion etching (DRIE), but due to its large elastic modulus, achieving angles of several degrees with small actuation torques requires beams long enough that weight bearing is limited. This also limits desirability of elastic bending joints based on other semiconductor materials or metals.

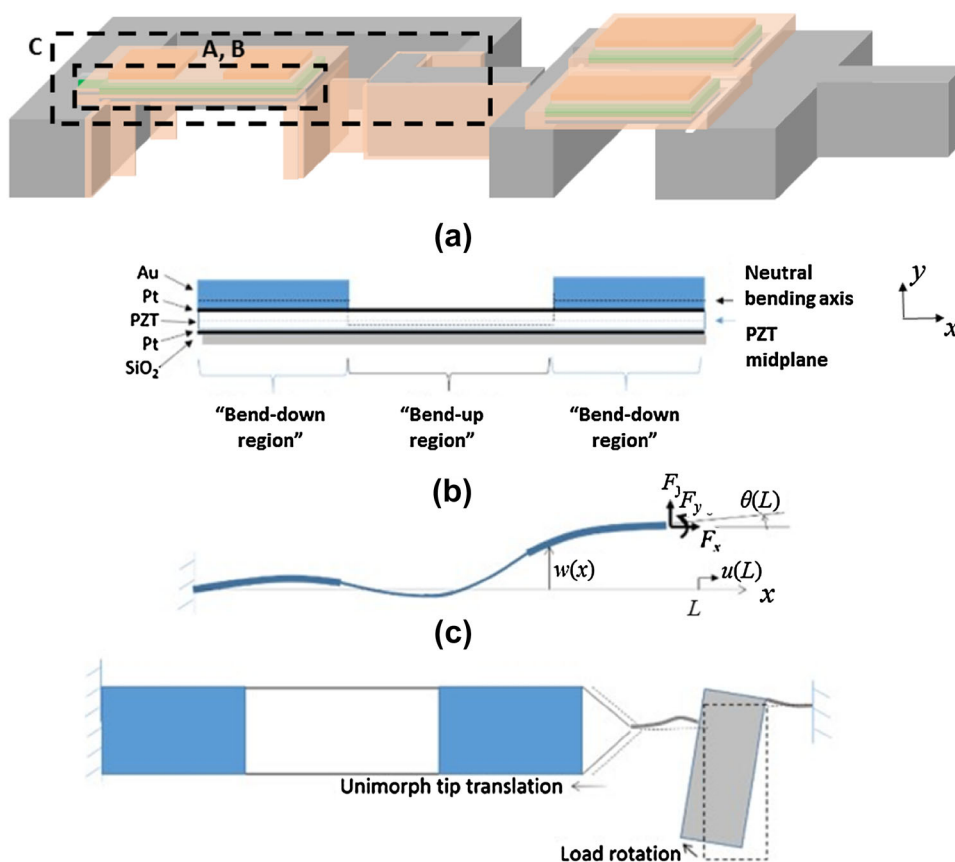
Parylene-C, in contrast, can achieve large bend angles with much shorter beams and actuating moments, which allows it to maintain substantial payloads so long as aspect ratios are respectable. In the current work, 23:1 aspect ratio is achieved, sufficient for greater out-of-plane stiffness than silicon or metal beams achieving comparable bend angles under input moment constraints. This ability is not unique to parylene-C: poly(methyl methacrylate) or PMMA, for example, used for high-aspect ratio photolithography, has been demonstrated to achieve even higher aspect ratios with a similar elastic modulus, though requiring X-ray lithography to do so. On the other hand, relative to high aspect ratio photopolymers such as PMMA and SU-8, parylene-C does support larger strains at yield and failure, which is advantageous for the resilience of fabricated structures, especially when many polymer elements are to be used in a single device.

### 2.3 In-plane rotation: piezoelectric actuator coupling

While Sect. 2.2 discusses why high-aspect ratio polymer beams may be desirable, it does not address how piezoelectric actuation force might be coupled to such beams for in-plane rotation. One method to do so is to attach a piezoelectric cantilever to a rigid element supported by the polymer beam at a slight offset. As a given piezoelectric cantilever will tend to deflect either upwards or downwards, as discussed in Sect. 2.1, piezoelectric beams for lateral actuation in this arrangement are constructed of a combination of bend-up and bend-down elements, shown schematically in Fig. 4a and b. Behavior for such beams, given perfect end constraints, has previously been presented in (Oldham et al. 2008).

In this work, parylene-C is used to construct both a thin parylene tether from the PZT beam to a rigid link being rotated, as well as the main elastic flexure, which is the primary weight bearing element and pivot point for rotation, with performance dependent on both in-plane and out-of-plane compliance. A typical rotational mechanism is shown in Fig. 4c. Although general trends with material selection and elastic flexure aspect ratio will follow those

**Fig. 4** **a** Schematic (*side view*) of bend-down/bend-up piezoelectric cantilever designed to generate in-plane tip displacement; **b** conceptual view of non-ideal cantilever bending in presence of residual stresses; **c** schematic (*top view*) of cantilever driving in-plane rotation of a load through coupling to a high-aspect ratio flexure with an offset flexible tether



discussed in Sect. 2.3, total motion of the combined rotational joint is more complex, depending on relative compliance of actuator, flexure, and tether components, in both in-plane and out-of-plane directions.

Generalizing cantilever bending for a bend-up/bend-down actuation element, the out-of-plane deformation of the piezoelectric unimorph,  $w$ , as a function of distance along the beam,  $x$ , is described by.

$$\frac{d^2w}{dx^2} = \frac{1}{(EI)_{comp}} [M_{act}(V, x) + M_R(x) + M_\theta - F_x(w(L) - w(x)) + F_y(L - x)] \tag{5}$$

where  $L$  is the unloaded beam length,  $(EI)_{comp}$  is the combined composite modulus and moment of inertia of the multi-layer thin-film laminate,  $M_{act}$  is the now a position dependent internal moment generated by the thin-film PZT layer,  $M_R$  is net residual stress in the PZT unimorph, and  $F_x, F_y$ , and  $M_\theta$  are external force and moment loads. Typically,  $M_{act}$  and  $M_R$  are constant through bend-up vs. bend-down segments, denoted as  $M_1$  and  $M_{R,1}$  vs.  $M_2$  and  $M_{R,2}$ , respectively.

The loaded length of the piezoelectric beam is governed by both contraction of the piezoelectric layer under an applied voltage and external axial loading. This length can be equated to the total length of the beam’s curved profile through arc length approximation, producing an equation for tip displacement,  $u(L)$ , in the  $x$ -direction,

$$L \left( 1 + \frac{d_{31,eff} \nu_{PZT} E_{PZT} w_{tPZT} + F_x}{(EA)_{comp}} \right) = \int_0^{L+u(L)} \sqrt{1 - \left( \frac{dw}{dx} \right)^2} dx \tag{6}$$

where  $(EA)_{comp}$  is the combined axial modulus and cross-sectional area of the multi-layer laminate.

The displacement of the actuator tip must match that of the elastic load under the same force, or,

$$\mathbf{F}_0 = \begin{bmatrix} F_x \\ F_y \\ M_\theta \end{bmatrix} = \mathbf{K} \begin{bmatrix} u(L) \\ w(L) \\ \theta(L) \end{bmatrix} = \mathbf{K} \mathbf{u}_0 \tag{7}$$

where  $\mathbf{F}_0$  is a vector containing the external forces at the actuator tip,  $\mathbf{K}$  is a stiffness matrix describing the resistance of the external load, and  $\mathbf{u}_0$  is a vector of lateral ( $u$ ), vertical ( $w$ ) and rotational ( $\theta$ ) tip displacements.

The total elastic resistance to the piezoelectric beam,  $\mathbf{K}$ , is based on dimensions of the compliant tether and rigid load, as well as the main elastic flexure. These elements are shown schematically in Fig. 5, with their analytical model provided in the Appendix. For a given design, once  $\mathbf{K}$  is calculated, Eqs. (5)–(7) can be solved numerically to evaluate actuator tip displacement under various forces and associated rigid load rotation.

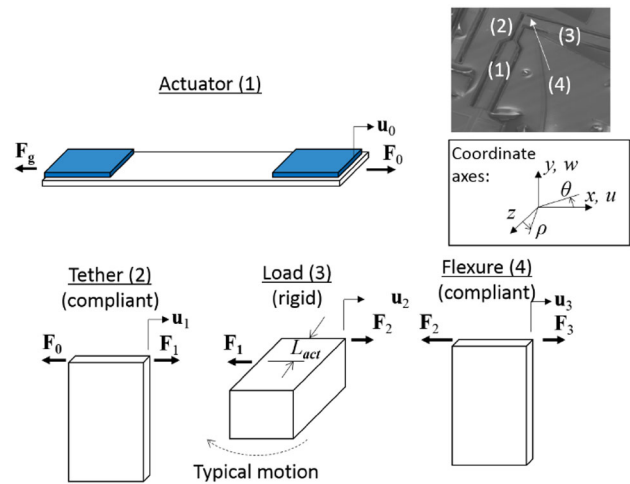


**Fig. 5** Elements of in-plane rotational actuator assembly used in compliant bending mechanism analysis (see Appendix)

Resulting actuation units only approach their maximum bend angle if the small stroke length of the PZT actuator can be as fully coupled to the bending mechanism as possible. This raises a second potential benefit of high-aspect ratio elastic flexures, though residual stresses in the PZT stack after fabrication are even more important. Under certain fabrication outcomes, sufficient initial curvature of the beam may increase nonlinear arc length effects of (6). In turn, this may increase the magnitude of in-plane translation of the PZT beam, as shown in Fig. 6. For example, upward-bending residual stress ( $M_R \approx M_1$  in Fig. 6) pre-bends the actuator in its direction of motion, amplifying nonlinear beam displacement by approximately 20–25% over an unstressed beam, with largest strokes reached with the largest out-of-plane to in-plane stiffness ratio of the flexure and tether.

### 2.4 Integrated leg and robot design

Robotic legs tested in this work are constructed from combinations of lateral and vertical actuation units described in Sects. 2.1, 2.2 and 2.3. The primary robot design evaluated is a hexapod design shown schematically in Fig. 7. Larger robots, such as the 30-leg “millipede” shown in Fig. 1, are generated by altering the number and location of legs and/or actuators in each leg.

The nominal hexapod design from Fig. 7 is 5 mm wide and 2.4 mm long, using three out-of-plane bending beams at each “knee” to generate vertical foot motion and one in-plane actuation assembly at each “hip” to generate lateral foot motion. Each out-of-plane actuator is 300  $\mu\text{m}$  long by 100  $\mu\text{m}$  wide. Anticipated rotation for each knee joint at 20 V with a 5.3  $\mu\text{m}$  parylene-C coating is 5.1° (see Fig. 3; Sect. 2.1). In-plane actuators were optimized with respect to parylene-C flexure and tether length and width to maximize in-plane rotation when using 750  $\mu\text{m}$  by 100  $\mu\text{m}$

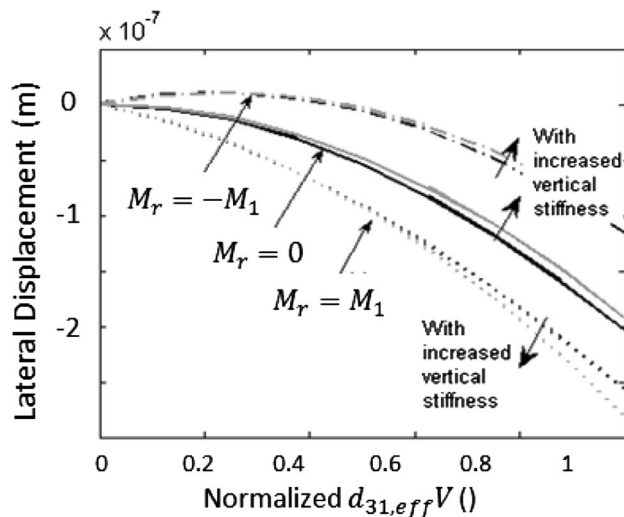


**Fig. 6** Lateral displacement of piezoelectric beam tip as a function of forcing under residual stress and out-of-plane load stiffness scenarios (actuation force normalized to  $d_{31,eff}V$ ) at 20 V to isolate nonlinear bending contributions from nonlinear piezoelectric forcing. Residual stress may increase ( $M_R > 0$ ) or decrease ( $M_R < 0$ ) actuator displacement due to pre-bending of the actuator; this effect is greatest when out-of-plane vertical stiffness is high

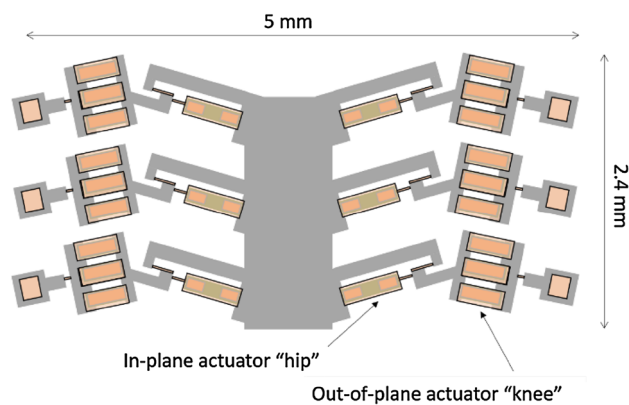


**Fig. 7** Schematic overhead layout of a hexapod prototype for in-chip micro-robot leg testing, combining out-of-plane (Sect. 2.1) and in-plane (Sect. 2.3) actuation units

wide piezoelectric bend-up/bend-down actuators. In-plane translation of the bend-up/bend-down PZT beams was anticipated to be 0.20–0.25  $\mu\text{m}$  at 20 V, dependent on residual stress levels after fabrication (see Fig. 6; Sect. 2.3). Acting across an optimized 4  $\mu\text{m}$  long moment arm offset between the parylene tether and flexure, this would produce in-plane rotation in the range of 2.9–3.6°.

### 3 Robot fabrication

Actuators and robots formed from integrated thin-film PZT actuators, silicon links, and parylene beams may be fabricated from silicon or silicon-on-insulator (SOI) wafers,

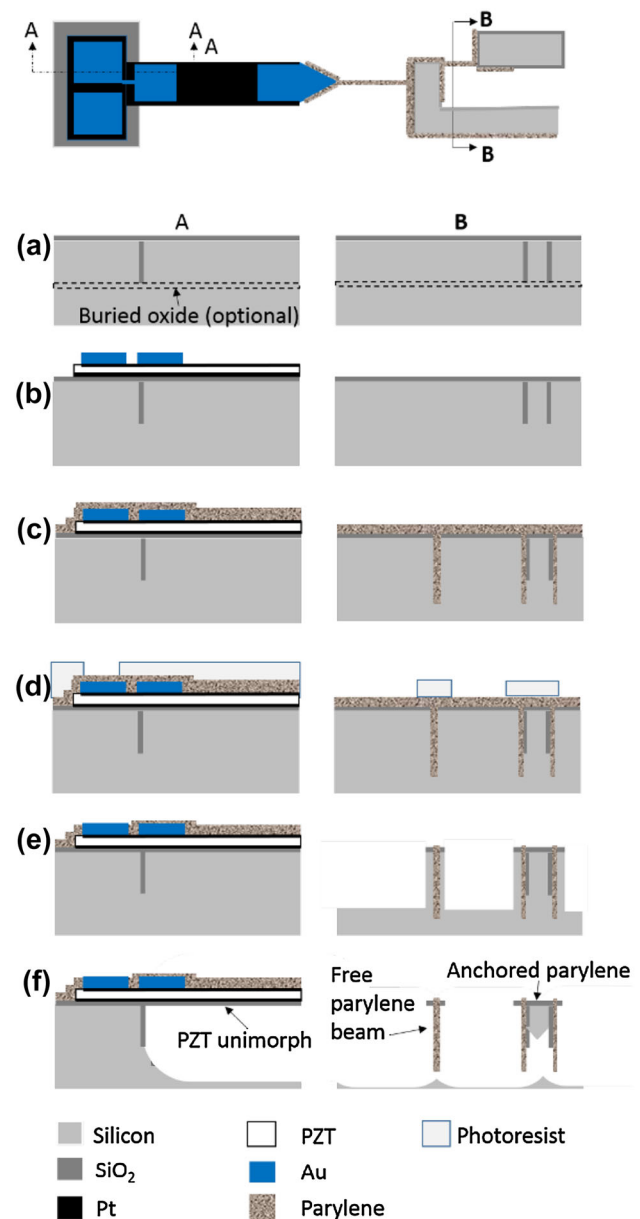


**Fig. 8** Actuation unit and robot prototype fabrication process: **a** silicon dioxide isolation trench refill on Si or optional SOI wafer; **b** thin-film PZT and Pt electrode deposition and patterning; **c** deep trench etching and parylene refill; **d** parylene lithography with timed photoresist/parylene etch; **e** deep trench etching for rough geometry definition; **f**  $\text{XeF}_2$  isotropic etch to complete Si removal

with key fabrication steps shown in Fig. 8. In the current work, SOI wafers with a 30  $\mu\text{m}$  thick device layer, and thus 30  $\mu\text{m}$  robot chassis thickness, are used. Rigid element geometry is pre-defined by deep-reactive ion-etching (DRIE) of narrow trenches that are refilled with TEOS silicon dioxide (Fig. 8a). These trenches, nominally 30  $\mu\text{m}$  deep and 3  $\mu\text{m}$  wide, protect free standing silicon elements from being damaged during eventual release steps, and also provide anchor points for the parylene film. Surface  $\text{SiO}_2$  is

removed by chemical mechanical polishing, followed by deposition of LPCVD high-temperature SiO<sub>2</sub> which serves as a high-quality elastic layer for thin-film PZT deposition.

A titanium oxide adhesion layer (40 nm), platinum electrode layers (bottom: 150 nm/top: 100 nm), a piezoelectric (PNZT, 4/20/80) seed layer, and thin-film PZT (1.0 μm combined) are deposited by a combination of electron beam evaporation and chemical solution deposition. For the devices tested, these deposition steps were performed by Radiant Technologies, Inc. (Evans and com 2001). Platinum and PZT layers are patterned by reactive-ion etching, followed by deposition of a patterned Ti/Au layer by lift-off for bond-pads and bend-down unimorph definition (Fig. 8b).

After PZT stack processing, locations of high-aspect parylene beams were defined by an additional DRIE etch. Chemical vapor deposition (CVD) of parylene-C then refills the trenches, with typical depth of 70 μm and trench widths ranging from 3 to 10 μm (Fig. 8c). Parylene deposition leaves a relatively thick (~5 μm) layer of parylene on the surface of the wafer. To pattern surface parylene, a thin protective silicon dioxide coating is deposited at low temperature by plasma enhanced chemical vapor deposition (PECVD), then photoresist is spin-coated to an approximately equal depth to that of the parylene on the surface, then patterned lithographically (Fig. 8d). A timed O<sub>2</sub> plasma RIE then etches through both exposed parylene and the patterning photoresist, exposing portions of the silicon wafer surface to be exposed for further patterning.

To release moving parts, additional DRIE trenches are etched, through either the entire exposed wafer surface after parylene etching or after an additional lithography step. These trenches are etched to a depth approximately equal to the parylene beams, cleaned with O<sub>2</sub> plasma, then exposed to XeF<sub>2</sub> gas to isotropically etch underneath rigid silicon and flexible parylene structures (Fig. 8e, f). If a bare silicon wafer is used, timed etching is required to avoid etching upward to the wafer surface during the XeF<sub>2</sub> etch; if a SOI wafer is used, the buried oxide layer acts as an etch stop, fully encapsulating silicon structures when combined with the initial silicon dioxide isolation trenches.

Sample structures generated by this process are shown in Fig. 9. Figure 9a shows a single completed in-plane actuator test structure, indicating locations of its PZT and parylene elements. Figure 9b shows the relative locations of the in-plane and out-of-plane elements in the simple hexapod prototype. Also shown in Fig. 9b are serpentine silicon springs used to make electrical connections between the silicon die and the PZT elements, and foot locations. Feet are manufactured by opening a significantly wider DRIE trench than other locations, which leads to deeper etching at those locations due to loading effects during the DRIE process. Feet are formed by the same coating of parylene-C applied to the remainder of the wafer, but to a

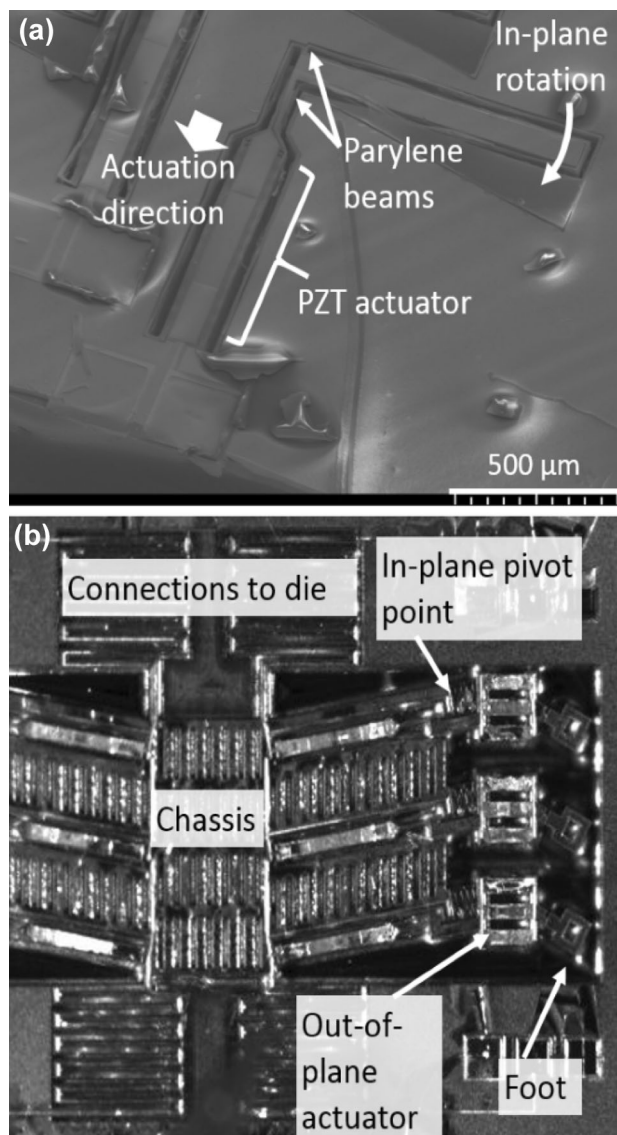


**Fig. 9** Sample (a) in-plane actuation mechanisms and (b) in-chip hexapod produced by the proposed thin-film PZT/parylene-C integration process

depth of approximately 150 μm as a result, vs. thicknesses of 30–70 μm elsewhere in the structure.

#### 4 Testing and results

An oblique detail image of one set of robotic feet in a hexapod prototype is shown in Fig. 10. Static deflections of in-plane and out-of-plane actuators were estimated from optical images by scaling motion against dimensions of known features at equivalent image depths. Measurements of dynamic leg motion were made using a laser Doppler vibrometer (LDV), shown in Fig. 11. To obtain a clear return of the laser, LDV measurements are made on the surface of the out-of-plane bending cantilevers, rather than

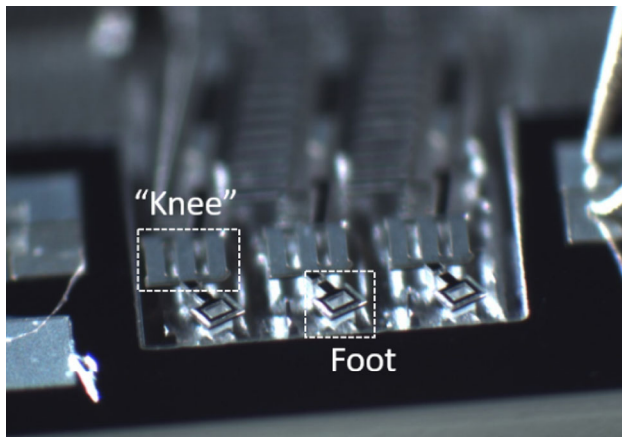


**Fig. 10** Optical microscope image of hexapod legs during actuator testing at 19 V

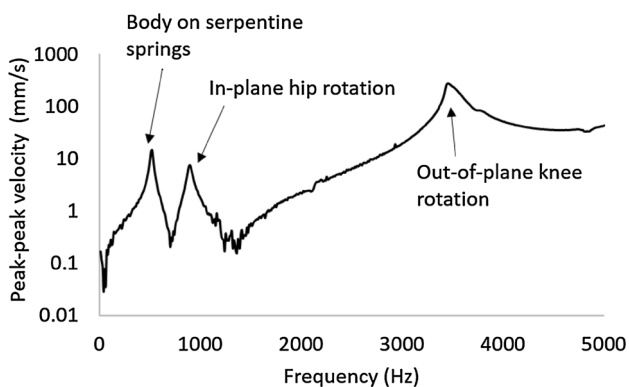


**Fig. 11** Frequency response, actuation voltage (4 V<sub>pp</sub>) to out-of-plane LDV velocity measurement taken from center of vertical actuators

the micro-robot foot. Although the LDV only directly measures out-of-plane motion, there is sufficient out-of-plane component to the nominally in-plane motions within the robot to obtain natural frequency information of those modes, though not their dynamic amplitudes. Frequency response was acquired under a swept sine excitation, with both actuators in a leg connected in parallel to the voltage source; the robot was suspended from ground by the silicon tethers used to apply voltage during this test.

Measured static rotations and natural frequencies of the robot joints are listed in Table 3. Static actuator and leg displacements are in agreement with model predictions, to within the resolution of our measurements. Predicted natural frequencies are about 5–7% lower than observed, implying less inertia than anticipated in the robot leg, possibly due to over-etching of openings used to form robot feet. It is also known that elastic modulus of a Piezoelectric film will vary under an applied voltage, but the magnitude of this effect is not well characterized for PZT thin films. Also of interest is that dynamic out-of-plane rotation achieves sufficient amplitudes at resonance

**Table 3** Predicted and observed robotic leg joint characteristics

	Predicted	Observed
Out-of-plane rotation	5.1°	4.9 ± 0.5°
Out-of-plane natural frequency (Hz)	3080	3300
In-plane rotation	2.9–3.6°	4.2 ± 1.4°
In-plane natural frequency (Hz)	862	895

to induce mild nonlinear softening effects caused by the rigid foot load moving over large angles. Other important characteristics of the fabricated structures are related to issues such durability, power consumption, and payload capacity. Adhesion strength between parylene films and silicon dioxide surfaces to which they are attached was estimated from dedicated test structures at 4.4 MPa, sufficiently large that failure of silicon dioxide/parylene interfaces was not observed in micro-robotic leg structures (Shin et al. 2014). Maximum static stress in the tether element at its thinnest point is estimated at 4.1 MPa, distributed over a larger area at the adhesion interface. Maximum static stress is larger in the vertical bending beams, due to the relatively large offset of the parylene surface from the neutral axis, but still estimated at 24 MPa using our laminate beam model, vs. an estimated parylene-C yield stress of 55 MPa from literature (Shih et al. 2003).

Total capacitance of piezoelectric elements in the hexapod design was approximately 0.3 nF, which is the primary determinant of power consumption for actuation, depending on the operating voltage and step frequency applied. While load-bearing capacity could not be directly measured for the fabricated structures, due to the presence of the silicon tethers for electrical power connections, relatively close agreement of resonant frequencies with analytical results suggests that bending models for actuator behavior should provide reasonable estimates for payload capacity, though again this will be affected choices of specific leg operating voltages and desired range-of-motion. Variability in leg electrical properties can also not be assessed individually, but based on experience with single actuator test structures, capacitance of individual legs is likely to vary by approximately 10%. This variation arises mostly from variation in parasitic capacitance at the electrical interconnects and bond pads, but in part from variations in PZT properties due to local variation in thermal environment experienced during fabrication.

## 5 Discussion

To examine the overall utility of robotic leg structures described in this paper, Table 4 compares hexapod prototype functionality to a selection of other small-scale robots

**Table 4** Comparison of legged micro-robot attributes

Quantity	Unit	Mohebbi et al. (2001)	Baisch and Wood (2011)	Murthy et al. (2012)	Kladitis and Bright (2000)	Ebefors et al. (1999)	Hollar et al. (2003)	This work	Projection with payload
Actuation		Electro-thermal	SMA	Electro-thermal	Electro-thermal	Electro-thermal	Electro-static	<b>Piezoelectric</b>	<i>Piezoelectric</i>
Size		30 × 10	17 × 23	10 × 10	10 × 10	10 × 10	8.5 × 4	<b>5 × 2.5</b>	5 × 2.5
Leg motion axes		x, z, $\theta_y$	$\theta_y, \theta_x$	z	x, z	$\Theta_x$	$\theta_x$	$\theta_y, \theta_x$	$\theta_y, \theta_x$
Leg angle	°	NA	9	NA	NA	20	90	<b>5</b>	3
Foot stroke	μm	5	640	20	3.8	340	400	<b>~70 (static)</b>	~40
Leg bandwidth	Hz	120	1	135	120	110	1	<b>880</b>	33
Chassis mass	mg	3.5 (est.)	95	3.8	32	80	6.4	<b>0.3</b>	0.3
Voltage	V	60	~4	10	5	18	50	<b>19</b>	19
Power	mW		280	750–	2870	175	0.1	<b>0.62</b>	0.024
Payload	mg	150	>9500	>10	3	2500	>10		9

from literature for which substantial performance information is available. Thin-film PZT/parylene hexapod capabilities are described both as tested and in a hypothetical loaded configuration, in which payload is added to analytical actuator models until free out-of-plane range of motion is reduced by approximately half. Leg bandwidth is then estimated from elastic joint models with the effective inertia from this payload added.

First, the most basic limitation of the thin-film PZT/parylene hexapod is that it is presently only a chassis with leg actuation, and issues of assembling power and computational elements to produce an autonomous system remain to be addressed. Regarding leg functionality, range of motion remains much smaller than is typical of macro-scale legged robots, and even of several existing micro-robots. On the other hand, leg stroke relative to body length is still respectable (2–3% vs. up to 5% in representative micro-robots). Estimated payload capacity is also quite small, on the order of 1–10 mg, but again quite respectable given robot size.

The key opportunities for the proposed robot architecture are related to its lightly damped, low-power actuation. Power consumption shown is provided for ideal capacitive loading with a square wave actuation voltage at the first robot natural frequency. With such small capacitive actuators, relatively low projected natural frequencies when carrying a payload result in power consumption on the order of just tens of microwatts. Divided by payload capacity, this corresponds to a required power density of just 5 W/kg, supposing that 50% of payload is allocated to power. Such low power density is critical at small scales, as effective power densities of sources generally decline as they become smaller. For example, power densities of solid-state Li-ion batteries can exceed 100 W/kg, but once packaging and other components are taken into account, effective power densities of existing millimeter-scale batteries are less than 10 W/kg (General Electronics Battery Co. 2011; Cymbet Corp. 2016). Even if higher power densities can be maintained in future micro-batteries, it is also true that substantial power may be required to accommodate sensing, computation, and inefficiencies of power electronics (Edamana and Oldham 2014; Oldham et al. 2011).

Low damping coefficients in integrated piezoelectric actuation elements become important because at low natural frequencies under payload and with modest static actuator stroke, opportunities for dynamic locomotion become critical. The damping ratio of resonant modes in the tested micro-robot range from 0.025 to 0.05, sufficient for an up to 10- to 20-fold increase in foot displacement near resonance. If lightly-damped resonant behavior can be leveraged with near-resonance running gaits, it may be possible to produce micro-robots with similarly improved

speed and/or even lower voltage and power requirements, as has been demonstrated in some macro- and meso-scaled systems (Qu and Oldham 2016; Birkmeyer et al. 2009; Pelc et al. 2008; Rios et al. 2017; Hariri et al. 2016). On the other hand, leveraging underdamped motion can be complicated by leg-to-leg mechanical and/or electrical variability. Robot mobility and/or speed might alternatively be enhanced by incorporating greater numbers of piezoelectric actuators into larger legs and/or robots, but with even more challenging implications for power and payload capacity.

## 6 Conclusions

Simple micro-robotic leg joint designs for in-plane and out-of-plane motion based on thin-film piezoelectric actuation have been presented, making use of benefits of polymer film integration in a high-aspect ratio micromachining process for parylene-C. Integrated into a simple robot test system on a silicon chip, leg assemblies demonstrate close agreement with modeled range-of-motion and bandwidth based on elastic structure modeling. Relative to other micro-robotic systems, resulting range-of-motion and payload capacity are modest, but respectable relative to robot size. Key potential advantages for long-term micro-robot development are extremely low piezoelectric actuator power consumption relative to force generation and hence payload capacity, and very low damping ratios that may support eventual high-speed, dynamic locomotion.

**Acknowledgements** The authors thank the National Science Foundation, Grants CMMI 0954422, IIS 1208233 and CMMI 1435222, and the Army Research Laboratory Summer Research Opportunities Program for support of this research.

## Appendix

Combined behavior of multiple polymer elements from in-plane rotation mechanisms is modeled by series of force balance, compliance, and geometric constraint equations for the elements previously introduced in Fig. 5. These equations are applied in up to five dimensions, neglecting torsion of beams in the parallel direction of the actuators (about the  $x$ -axis as defined in Fig. 5). Force balances about the individual components can be summarized as

$$\mathbf{F}_1 = \mathbf{T}_1 \mathbf{F}_0, \mathbf{F}_2 = \mathbf{T}_2 \mathbf{F}_1, \mathbf{F}_3 = \mathbf{T}_3 \mathbf{F}_1 \quad (8)$$

where  $\mathbf{F}_0$  is the input force from the piezoelectric beam and  $\mathbf{F}_1$ ,  $\mathbf{F}_2$ , and  $\mathbf{F}_3$  are the force vectors at the right-hand side of the elements (tether, rigid link, and tether respectively), where  $\mathbf{T}_1$ ,  $\mathbf{T}_2$ , and  $\mathbf{T}_3$  are matrices computing static force balances from forces on the left-hand side of the elements in their neutral position, i.e.

$$\mathbf{T}_1 = \begin{bmatrix} 1 & 0 & 0 & 0 & 0 \\ 0 & 1 & 0 & 0 & 0 \\ 0 & -L_t & 1 & 0 & 0 \\ 0 & 0 & 0 & 1 & 0 \\ 0 & 0 & 0 & L_t & 1 \end{bmatrix}, \quad (9)$$

$$\mathbf{T}_2 = \begin{bmatrix} 1 & 0 & 0 & 0 & 0 \\ 0 & 1 & w_b & 0 & 0 \\ 0 & 0 & 1 & 0 & 0 \\ 0 & 0 & 0 & 1 & -w_b \\ 0 & 0 & 0 & 0 & 1 \end{bmatrix}$$

where  $L_t$  is the tether length,  $w_b$  is the width of the rigid link, and  $\mathbf{T}_3$  is identical to  $\mathbf{T}_1$  but using flexure dimensions.

Deformation of the elastic parylene elements is calculated as the difference between tip positions and their projected neutral location based on their initial rotation angles,

$$\mathbf{u}_3 - \mathbf{V}_f \mathbf{u}_2 = \mathbf{C}_f \mathbf{F}_3$$

$$\mathbf{u}_1 - \mathbf{V}_t \mathbf{u}_0 = \mathbf{C}_t \mathbf{F}_1 \quad (10)$$

where  $\mathbf{u}_1$  and  $\mathbf{u}_3$  are tip displacements of the tether and flexure, respectively (with  $\mathbf{u}_3 = \mathbf{0}$  when anchored to the substrate). In (10),  $\mathbf{V}_f$  and  $\mathbf{V}_t$  are matrices projecting the neutral position of the tether and flexure tips given rotation of earlier links, and  $\mathbf{C}_f$  and  $\mathbf{C}_t$  are compliance matrices for the tether and flexure, respectively. Projection matrices are given by

$$\mathbf{V}_1 = \begin{bmatrix} 1 & 0 & 0 & 0 & 0 \\ 0 & 1 & L_t & 0 & 0 \\ 0 & 0 & 1 & 0 & 0 \\ 0 & 0 & 0 & 1 & -L_t \\ 0 & 0 & 0 & 0 & 1 \end{bmatrix}, \quad (11)$$

$$\mathbf{V}_2 = \begin{bmatrix} 1 & 0 & 0 & 0 & 0 \\ 0 & 1 & L_f & 0 & 0 \\ 0 & 0 & 1 & 0 & 0 \\ 0 & 0 & 0 & 1 & -L_f \\ 0 & 0 & 0 & 0 & 1 \end{bmatrix}$$

with  $L_f$  being the flexure length. The compliance matrix for the flexure in the tether-flexure assembly is calculated from simple Bernoulli bending theory with a simple shear stress adjustment in the  $y$ -direction,

$$\mathbf{C}_f = \begin{bmatrix} \frac{L_f}{E_p A_f} & 0 & 0 & 0 & 0 \\ 0 & \frac{L_f^3}{3E_p I_{f,z}} + \frac{L_f}{G_p A_f} & \frac{L_f^2}{2E_p I_{f,z}} & 0 & 0 \\ 0 & \frac{L_f^2}{2E_p I_{f,z}} + \frac{1}{G_p A_f} & \frac{L_f}{E_p I_{f,z}} & 0 & 0 \\ 0 & 0 & 0 & \frac{L_f^3}{3E_p I_{f,y}} & \frac{L_f^2}{2E_p I_{f,y}} \\ 0 & 0 & 0 & \frac{L_f^2}{2E_p I_{f,y}} & \frac{L_f}{3E_p I_{f,y}} \end{bmatrix} \quad (12)$$

where  $A_f$  is the flexure's cross-sectional area,  $I_f$  is its area moment of inertia about  $z$  or  $y$  axes, and  $E_p$  and  $G_p$  are the elastic and shear moduli of parylene-C, respectively.

Geometric constraints for the rigid element are compiled in matrix form,

$$\mathbf{u}_2 = \mathbf{S}_2 \mathbf{u}_1 \quad (13)$$

where  $\mathbf{S}_2$  is a matrix projecting displacement at  $\mathbf{u}_2$  from  $\mathbf{u}_1$  for small angular rotations,

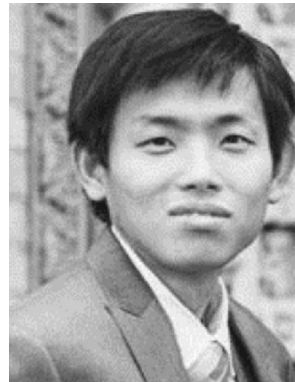
$$\mathbf{S}_2 = \begin{bmatrix} 1 & 0 & 0 & 0 & -L_{act} \\ 0 & 1 & w_b & 0 & 0 \\ 0 & 0 & 1 & 0 & 0 \\ 0 & 0 & 0 & 1 & -w_b \\ 0 & 0 & 0 & 0 & 1 \end{bmatrix} \quad (14)$$

Equations (8)–(14) can be solved by linear algebra to either relate a specified input force to a multi-axis displacements of the flexure and tether endpoints and rigid link, or more generally to calculate the combined stiffness matrix,  $\mathbf{K}$ , used to calculate actuator displacement numerically when accounting for nonlinear arc lengths effects introduced in (5)–(7) in Sect. 2.3.

## References

- Aktakka, E.E., Woo, J.K., Egert, D., Gordenker, R., Najafi, K.: A Vibratory Stage for on Chip Physical Stimulation and Calibration of MEMS Gyroscopes. IEEE ISISS, Laguna Beach (2014)
- Ash, B.J., Stone, J., Roger, D.F., Schadler, L.S., Siegel, R.W., Benicewicz, B.C., Apple, T.: Investigations into the Thermal and Mechanical Behavior of PMMA/Alumina Nanocomposites. Proc. MRS, Boston (2001)
- Baisch, A., Wood, R.: Design and fabrication of the Harvard ambulatory micro-robot. Robot. Res. **70**, 715–730 (2011)
- Baumeister, G., Mueller, K., Ruprecht, R., Hausselt, J.: Production of metallic high aspect ratio microstructures by microcasting. Microsyst. Technol. **8**(2), 105–108 (2002)
- Becker, H., Heim, U.: Hot embossing as a method for fabrication of polymer high aspect ratio structures. Sens. Actuators **83**, 130–135 (2000)
- Bergbreiter, S., Pister, K.: Design of an Autonomous Jumping Microrobot. IEEE ICRA, Rome (2007)
- Birkmeyer, P., Petersen, K., Fearing, R.S.: DASH: A Dynamic 16 g Hexapedal Robot. IEEE/RSJ ICRS, St. Louis (2009)
- Cymbet Corp.: Enerchip rechargeable solid state bare die batteries. <http://www.cymbet.com> (2016)
- Conway, N.J., Traina, Z.J., Kim, S.-G.: A strain amplifying piezoelectric MEMS actuator. J. Micromech. Microeng. **17**, 781–787 (2007)
- Dellmann, L., Roth, S., Beuret, C., Racine, G., Lorenz, H., Despont, M., Renaud, P., Vettiger, P., de Rooij, N.: Fabrication Process Of High-Aspect Ratio Elastic Structures For Piezoelectric Motor Applications. Transducers, Chicago (1997)
- Ebefors, T., Mattsson, Kalvesten, J.E., Stemme, G.: A walking silicon micro-robot. Proceedings of the 10th International Conference on Solid-State Sensors Actuators, pp. 1202–1205, Sendai (1999)
- Edamana, B., Oldham, K.R.: A near-optimal sensor scheduling strategy for an on-off controller with an expensive sensor. IEEE/ASME T Mech. **19**(1), 158–170 (2014)
- Edamana, B., Hahn, B., Pulskamp, J.S., Polcawich, R.G., Oldham, K.: Modeling and optimal low-power on-off control of thin-film piezoelectric rotational actuators. IEEE/ASME Trans. Mech. **16**(5), 884–896 (2011)
- Erdem, E.Y., Chen, Y.-M., Mohebbi, M., Suh, J.W., Kovacs, G.T.A., Darling, R.B., Bohringer, K.F.: Thermally-actuated omnidirectional walking microrobot. J MEMS **19**(3), 433–442 (2010)
- Espinosa, H.D., Prorok, B.C.: Size effects on the mechanical behavior of gold thin films. J. Mat. Sci. **38**, 4125–4128 (2003)
- Evans, J.: PZT-silicon cantilever benders. <http://www.ferrodevices.com> (2001)
- Fu, Y., Harvey, E., Ghantasala, M., Spinks, G.: Design, fabrication, and testing of piezoelectric polymer PVDF microactuators. Smart Mat. Struct. **15**(1), S141 (2005)
- General Electronics Battery Co., Ltd.: Produce specification (for high discharge ratio battery). <http://www.powerstream.com> (2011)
- Guerre, R., Drechsler, U., Bhattacharyya, D., Rantakati, P., Stutz, R., Heikkilä, T., Kirby, P.B., Despont, D.: Wafer-level transfer technologies for PZT-Based RF MEMS Switches. J. MEMS **19**(3), 548–560 (2010)
- Hariri, H., Prasetya, L.A., Foong, S., Soh, G.S., Otto, K.N., Wood, K.L.: A tether-less legged piezoelectric miniature robot using bounding gait locomotion for bidirectional motion. IEEE ICRA, Stockholm (2016a)
- Hariri, H., Prasetya, L.A., Soh, G.S., Wood, K.L.: Tether-less legged piezoelectric miniature robot using bounding gait locomotion for bidirectional motion. IEEE ICRA, Stockholm (2016b)
- Hollar, S., Flynn, A., Bellew, C., Pister, K.: Solar Powered 10 mg Silicon Robot. IEEE C, MEMS (2003)
- Hollar, S., Flynn, A., Bergbreiter, S., Pister, K.S.J.: Robot leg motion in a planarized-SOI, two-layer poly-Si process. J MEMS **14**(4), 725–740 (2005)
- Kim, B., Ryu, J., Jeong, Y., Tak, Y., Kim, B., Park, J.-O.: A ciliary Based 8-Legged Walking Micro Robot Using Cast IPMC Actuators. IEEE ICRA, Taipei (2003)
- Kladitis, P.E., Bright, V.M.: Prototype microrobots for micro-positioning and micro-unmanned vehicles. Sensors Actuators **80**, 132–137 (2000)
- Lam, T., Lam, K., Chan, H.: Micromachined piezoelectric polymer membrane acoustic sensor. Integr. Ferroelec. **76**(1), 31–37 (2005)
- Liu, G., Tian, Y., Kan, Y.: Fabrication of high-aspect-ratio microstructures using SU8 photoresist. Microsyst. Technol. **11**, 343–346 (2005)
- Lu, B.: Parylene as a new membrane material for biomems applications. California Institute of Technology, Pasadena (2012)
- Luo, Y., Lu, M., Cui, T.: A polymer-based bidirectional micropump driven by a PZT bimorph. Microsyst. Tech. **17**, 403–409 (2011)
- Ma, K., Chirarattananon, P., Fuller, S.W.R.: Controlled flight of a biologically inspired, insect-scale robot. Science **340**(6132), 603–607 (2013)
- Mohebbi, M.H., Terry, M.L., Bohringer, K.F., Kovacs, G.T.A., Suh, J.W.: Omnidirectional Walking Microrobot Realized By Thermal Microactuator Arrays. ASME IMECE, New York (2001)
- Murthy, R., Stephanou, H.E., Popa, D.: AFAM: an articulated four axes micro-robot for nanoscale applications. IEEE Trans. Automat. Sci. Eng. **10**(2), 276–284 (2012)
- Navarre, A., Rocks, S., Dewey, R.: Micromoulding of lead zirconate titanate (PZT) structures for MEMS. J. Electroceram. **19**, 321–326 (2007)

- Nemirovsky, Y., Nemirovsky, A., Muralt, P., Setter, N.: Design of a novel thin-film piezoelectric accelerometer. *Sensors Actuators A* **50**, 239–249 (1996)
- Oldham, K., Pulskamp, J.S., Polcawich, R.G., Dubey, M.: Thin-film piezoelectric lateral actuators with extended stroke. *J. MEMS* **17**(4), 890–899 (2008)
- Oldham, K., Edamana, B., Hahn, B.: Coordinated voltage conversion and low-power micro-actuator switching. ASME DSCC, Arlington (2011)
- Owen, K.J., VanDerElzen, B., Peterson, R.L., Najafi, K.: High Aspect Ratio Deep Silicon Etching. IEEE C. MEMS, Paris (2012)
- Park, J., Lee, S., Cho, J., Jung, S., Han, J., Kang, S.: Acoustic and electromechanical properties of 1-3 PZT composites for ultrasonic transducer arrays fabricated by sacrificial micro PMMA mold. *Sensors Actuators A* **108**, 206–211 (2003)
- Pelc, E.H., Daley, M.A., Ferris, D.P.: Resonant hopping of a robot controlled by an artificial neural oscillator. *Bioinspiration Biomim.* **3**(2), 026001 (2008)
- Pulskamp, J.: Millimeter-scale MEMS Enabled Autonomous Systems: System Feasibility and Mobility. SPIE, Baltimore (2012)
- Qu, J., Oldham, K.: Multiple Mode Dynamic Model for Piezoelectric Micro-Robot Walking. ASME IDETC, Charlotte (2016)
- Rasmussen, J., Bonivert, W., Krafcik, J. High Aspect Ratio Metal MEMS (LIGA) Technologies For Rugged, Low-Cost Firetrain And Control Components, NDIA 47th Fuze Conference (2003)
- Rhee, C.H., Pulskamp, J.S., Polcawich, R.G., Oldham, K.R.: Multi-degree-of-freedom thin-film PZT-actuated microrobotic leg. *J. MEMS* **21**(6), 1492–1503 (2012)
- Rios, S.A., Fleming, A.J., Yong, Y.K.: Design and Characterization of a Miniature Monolithic Piezoelectric Hexapod Robot. IEEE AIM, Banff (2016)
- Rios, S.A., Fleming, A.J., Yong, Y.K.: Miniature resonant ambulatory robot. *IEEE Robot. Autom. Lett.* **2**, 337–343 (2017)
- Ritter, T., Geng, X., Shung, K.K., Lopath, P.D., Park, S.-E., Shrout, T.R.: Single crystal PZT/Polymer composites for ultrasound transducer applications. *IEEE Trans. Ultrasonics* **47**(4), 792–800 (2002)
- Robin, C., Vishnoi, A.: Mechanical behavior and anisotropy of spin-coated SU-8 thin-film for MEMS. *J. MEMS* **23**(1), 168–180 (2013)
- Sanuy, A., Casanova, R., Dieguez, A., Samitier, J., Szymanski, M., Worn, H.: Energy Efficient HW/SW Integration in an Autonomous Microrobot: 12th World Multi-C. Systemics Cybernetics Informatics, Orlando (2008)
- Selvarasah, S., Chao, S.H., Chen, C.-L., Mao, D., Hopwood, J., Ryley, S., Sridar, S., Khademhosseini, A., Busnaina, A., Dokmeci, M.R.: A high aspect ratio, flexible, transparent and low-post parylene-C shadow mask technology for micropatterning applications. *Solid State Sensors Actuators Microsyst. C*, Lyon (2007)
- Shareef, I.A., Rubloff, G.W., Anderle, M., Gill, W.N., Cotte, J., Kim, D.H.: Subatmospheric chemical vapor deposition ozone/TEOS process for SiO<sub>2</sub> trench filling. *J. Vac. Sci. Technol.* **13**(4), 1888–1895 (1995)
- Sharpe Jr., W.N., Gianola, P.J.D.S., Eberl, C., Polcawich, R.G., Thompson, R.J.: Strain measurements of silicon dioxide microspecimens by digital image processing. *Exp. Mech.* **5**(649–658), 47–50 (2006)
- Shih, V.C.-Y., Harder, T.A., Tai, Y.C.: Yield Strength of Thin-Film Parylene-C, Symp. MEMS/MOEMS (DTIP), Cote D'Azur (2003)
- Shin, M., Choi, J., Rudy, R.Q., Kao, C., Pulskamp, J.S., Polcawich, R.G., Oldham, K.R.: Micro-robotic Actuation Units Based On Thin-Film Piezoelectric and High-Aspect Ratio Polymer Structures. ASME IDETC, Buffalo (2014)
- Sugita, K., Daisuke, T., Ono, S., Chiba, S., Iwata, K., Han, Y., Takato, M., Uchikoba, F., Saito, K.: SMA Actuator and Pulse-Type Hardware Neural Networks IC for Fat Walking Motion Of Insect-Type MEMS Microrobot. IEEE AIM, Banff (2016)
- Suzuki, Y., Tai, Y.: Micromachined high-aspect ratio parylene spring and its application to low-frequency accelerometers. *J. MEMS* **15**(5), 1364–1370 (2006)
- Timpano, K.: Mechanical Characterization of Gold Thin Films for RF MEMS. Proc. Virginia Space Grant Consortium Student Conf., Richmond (2005)
- Venkatragavaraj, E., Satish, B., Vinod, P., Vijaya, M.: Piezoelectric properties of ferroelectric PZT-polymer composites. *J. Phys. D Appl. Phys.* **34**(4), 487–494 (2000)
- Vogtmann, D.E., Gupta, S.K., Bergbreiter, S.: Multi-Material Compliant Mechanisms for Mobile Millirobots. IEEE ICRA, Shanghai (2011)
- Wang, Q.-W., Cross, L.E.: Constitutive equations of symmetrical trilayer piezoelectric benders. *IEEE Trans Ultrasonics, Ferroelec. Freq. Control* **46**(6), 1343–1352 (1999)
- Wilson, C.J., Ormeggi, A., Narbutovskih, M.: Fracture testing of silicon micro-cantilever beams. *J. Appl. Phys.* **5**, 142–150 (1996)



**Jongsoo Choi** received the B.S., M.S., and Ph.D. degrees in Mechanical Engineering from the University of Michigan, Ann Arbor, in 2010, 2011, and 2017, respectively. He is currently with Vesper Technologies, Boston, MA. Research interests include design, modeling, and fabrication of micro-scale sensors and actuators.



**Minchul Shin** received the B.S degree from Kyungpook National University, Daegu, Korea, in 2005, the M.S degree from University of Alabama at Birmingham, and the Ph.D. degree from the Tufts University in 2012, specializing in Microelectromechanical Systems (MEMS) and Micro/Nano Fabrication. Following his Ph.D. he worked as a postdoctoral fellow at the University of Michigan with a research concentration on thin film micro-robot design. He is currently an Assistant Professor with the Department of Mechanical Engineering at Georgia Southern University, Statesboro, GA. His research interests lie in MEMS design, sound source detection, micro-robotics and soft robot design.



**Ryan Q. Rudy** received the B.S.E. and M.S.E. degrees in Mechanical Engineering from the University of Michigan, Ann Arbor, in 2009 and 2010, respectively, and the Ph.D. Degree from the University of Maryland in 2014. He is currently a staff at the U.S. Army Research Laboratory in Adelphi, MD. Research interests include thin-film piezoelectric resonators, actuators, and micro-motors.



**Christopher Kao** received the B.S. degree in Movement Science from the University of Michigan in 2013, where he also studied engineering and psychology. He is currently attending the University of Virginia Medical School, with an interest in Emergency Medicine.



**Jeffrey S. Pulskamp** received the B.S. degree in Mechanical Engineering from the University of Maryland, College Park, in 2000. He is currently a MEMS Design and Mechanical Engineer with the Micro and Nano Materials and Devices Branch, U.S. Army Research Laboratory, Adelphi Laboratory Center, Adelphi, MD. His current research interests include RF MEMS devices, electromechanical design and modeling of MEMS, and millimeter-scale

robotics.



**Ronald G. Polcawich** received the B.S. degree in materials science and engineering from Carnegie Mellon University, Pittsburgh, PA, in 1997, and the M.S. degree in materials and the Ph.D. degree in materials science and engineering from The Pennsylvania State University, University Park, in 1999 and 2007, respectively. He is currently a Staff Researcher with the Micro and Nano Materials and Devices Branch, U.S. Army Research Laboratory, Adelphi

Laboratory Center, Adelphi, MD, where he is also currently the Team Lead for the RFMEMS and millimeter-scale robotics programs. The current research programs include switches and phase shifters for phased array antennas, tunable MEMS resonators/filters for secure communication, and mobile unattended sensor platforms. His research activities include materials processing of lead zirconate titanate (PZT) thin films, MEMS fabrication, RF components, MEMS actuator technologies, mm-scale robotics, MEMS inertial sensors, and sensors for aiding inertial systems.



**Kenn R. Oldham** is an Associate Professor of Mechanical Engineering at the University of Michigan. He received the Ph.D. in Mechanical Engineering from the University of California at Berkeley in 2006 and the B.S. in Mechanical Engineering from Carnegie Mellon University in 2000. His research focuses on the intersection of control systems and micro-scale sensing and actuation, with interests in design for controllability, optimal and robust

control, microsystem estimation and identification, and novel sensor and actuator design. Applications include terrestrial micro-robotics, endoscopic microscopy, and inertial and physiological sensing.